



**HAL**  
open science

## Orientation dependent recovery in strongly deformed Al-0.1% Mn crystals

Adeline Albou, Andras Borbely, Claire Maurice, Julian Haworth Driver

► **To cite this version:**

Adeline Albou, Andras Borbely, Claire Maurice, Julian Haworth Driver. Orientation dependent recovery in strongly deformed Al-0.1% Mn crystals. Philosophical Magazine, 2011, pp.1. 10.1080/14786435.2011.600733 . hal-00723597

**HAL Id: hal-00723597**

**<https://hal.science/hal-00723597>**

Submitted on 11 Aug 2012

**HAL** is a multi-disciplinary open access archive for the deposit and dissemination of scientific research documents, whether they are published or not. The documents may come from teaching and research institutions in France or abroad, or from public or private research centers.

L'archive ouverte pluridisciplinaire **HAL**, est destinée au dépôt et à la diffusion de documents scientifiques de niveau recherche, publiés ou non, émanant des établissements d'enseignement et de recherche français ou étrangers, des laboratoires publics ou privés.



**Orientation dependent recovery in strongly deformed Al-0.1% Mn crystals**

Journal:	<i>Philosophical Magazine &amp; Philosophical Magazine Letters</i>
Manuscript ID:	TPHM-11-Jan-0022.R2
Journal Selection:	Philosophical Magazine
Date Submitted by the Author:	08-Jun-2011
Complete List of Authors:	Albou, Adeline; Ecole des Mines de Saint Etienne, Materials Borbely, Andras; Ecole des Mines de Saint Etienne, Materials Maurice, Claire; Ecole des Mines de Saint Etienne Driver, Julian; Ecole des Mines de Saint Etienne, Materials
Keywords:	aluminium, crystals, recovery, hardness, EBSD, X-ray diffraction, dislocation structures
Keywords (user supplied):	orientation gradients

SCHOLARONE™  
Manuscripts

1  
2  
3 **Orientation dependent recovery in strongly deformed Al-0.1% Mn crystals**  
4

5  
6 **Adeline Albou<sup>a, b</sup>, Andras Borbely<sup>a</sup>, Claire Maurice<sup>a</sup> and Julian H. Driver<sup>a</sup>**  
7  
8

9  
10 <sup>a</sup> SMS Materials Centre and CNRS UMR 5146, Ecole des Mines de Saint Etienne, 158  
11 Cours Fauriel, 42023 Saint Etienne, France  
12

13 <sup>b</sup> Université Catholique de Louvain, Laboratoire IMMC/IMAP, Place Sainte-Barbe 2, 1348  
14 Louvain la Neuve, Belgium  
15  
16

17  
18 Corresponding author: Julian Driver

19 Tel + 33 477 420196, fax +33 477 420157

20 e-mail addresses: [adeline.albou@uclouvain.be](mailto:adeline.albou@uclouvain.be), [borbely@emse.fr](mailto:borbely@emse.fr), [maurice@emse.fr](mailto:maurice@emse.fr),  
21 [driver@emse.fr](mailto:driver@emse.fr).  
22  
23  
24  
25  
26  
27  
28  
29  
30  
31  
32  
33  
34  
35  
36  
37  
38  
39  
40  
41  
42  
43  
44  
45  
46  
47  
48  
49  
50  
51  
52  
53  
54  
55  
56  
57  
58  
59  
60

## Orientation dependent recovery in strongly deformed Al-0.1% Mn crystals

A. Albou<sup>a</sup>, A. Borbely<sup>a</sup>, C. Maurice<sup>a</sup> and J H Driver<sup>a</sup>

<sup>a</sup>SMS Materials Centre and CNRS UMR 5146, Ecole des Mines de Saint Etienne, 158  
Cours Fauriel, 42023 Saint Etienne, France

Single crystals of Al-0.1%Mn have been channel-die compressed to a true strain of 2.3 and their recovery behaviour at 240-320°C investigated by microhardness measurements, EBSD microtexture mapping and X-ray line broadening analysis. The crystal orientations are the nominally stable Goss {110}<001>, brass {110}<112> and S {123}<634>. For all three orientations the microhardness decreases with a logarithmic time dependency but the instantaneous recovery rates of the Brass oriented crystals are systematically lower than those of the other two orientations by a factor of about 2. The dislocation densities decrease rapidly in the first stages of recovery (<1 min) by dislocation dipole annihilation and more slowly thereafter. In the Goss and S orientations the later stage of recovery is due to sub-grain growth. The orientation dependency is ascribed to the relatively low misorientations developed by plastic straining in the Brass crystals (average about 4°) compared with the Goss and S orientations (about 7-8°).

Keywords: Recovery, aluminium, single crystals, dislocation substructure, orientation gradients

### 1. Introduction

For the case of fcc metals grain orientation is known to have a strong effect on both deformation microstructures and work hardening rates, see for example references [1-4]. It is often considered that grain orientation would also affect recovery rates but there have been very few studies of this problem after large strains, with the notable exception of cube oriented grains in rolled fcc metals. For this particular case Ridha and Hutchinson [5] proposed that plane strain compressed cube grains, by virtue of their weakly interacting dislocations with orthogonal Burger's vectors, recover rapidly to become potential nuclei for recrystallization. It can also be noted that Huang et al [6] have observed that the orientation gradients that can develop in hot deformed cube crystals are zones of high sub-grain coarsening rates and therefore recovery. One of the few studies of orientation dependent recovery on polycrystals is that of Xing et al [7] who characterized the grain structures of cold

1  
2  
3 rolled and lightly annealed aluminium by TEM. They observed that the lamellar bands (of  
4 elongated grains) of the rolling texture components exhibited significantly less coarsening  
5 than the bands of the other orientations.  
6  
7

8 It is difficult to assess orientation dependency in deformed polycrystals but the use of single  
9 crystals facilitates controlled, systematic studies. Previous studies on single crystals have been  
10 limited to relatively small deformations in tension, e.g. by Kuhlmann et al [8] and Hasegawa  
11 and Kocks [9] on aluminium crystals. The present work aims to characterise the influence of  
12 orientation after large strains typical of a cold rolled fcc metal. Since strong deformation, as in  
13 cold rolling, leads to grains converging on the rolling texture components (Goss  $\{110\}\langle 001\rangle$ ,  
14 brass  $\{110\}\langle 112\rangle$ , S  $\{123\}\langle 634\rangle$  and copper  $\{112\}\langle 111\rangle$  in fcc metals) it is of interest, and  
15 also more practicable, to examine the recovery behaviour of these orientations. It turns out  
16 that the copper orientation tends to develop micro-shear bands [2] which can rapidly become  
17 recrystallization nuclei [10] on light annealing and thereby limit the extent of recovery in this  
18 orientation. Consequently the present study has focussed on the 3 nominally stable  
19 orientations, namely Goss, Brass and S.  
20  
21  
22  
23  
24  
25  
26  
27  
28  
29

30 An alloy composition of 0.1wt%Mn was chosen since the Mn offers some solute hardening  
31 and solute drag to slow down recovery compared with pure Al. The sub-grain coarsening rates  
32 of this polycrystalline alloy have also been studied by Barou et al. [11, 12] Single crystals  
33 of the above three orientations were deformed to strains of 2.3 (thickness reductions of 90%)  
34 by plane strain compression and then samples lightly annealed to investigate recovery by  
35 hardness measurements, X-ray line profile analysis and EBSD orientation mapping.  
36  
37  
38  
39  
40  
41

## 42 2. Experimental Procedures

43 The material was a high purity Al-0.1wt% Mn alloy cast at the Alcan Voreppe research centre  
44 in the form of a 5 kg ingot. The impurities in the as-cast ingot were 6 ppm Si, 5 ppm Fe, 2  
45 ppm Mg and 15 ppm Cu. The ingot was processed to bars which were used for single crystal  
46 preparation by horizontal directional solidification. The single crystal bars of composition  
47 0.12 wt.%Mn and typical width 25mm were homogenised at 630°C for 24 hours. Single  
48 crystal samples with orientations  $\{110\}\langle 001\rangle$ ,  $\{110\}\langle 112\rangle$  and  $\{123\}\langle 63-4\rangle$  were carefully  
49 cut from the bars by spark erosion to dimensions of 6.95 x 8 x 10 mm (width, length, height).  
50  
51  
52  
53  
54  
55  
56  
57  
58  
59  
60

Room temperature plane strain compression was carried out in a channel-die using a  
servo-hydraulic Schenck machine at constant strain rate ( $10^{-2} \text{ s}^{-1}$ ) up to a true strain ( $\epsilon = -$

1  
2  
3  
4  
5  
6  
7  
8  
9  
10  
11  
12  
13  
14  
15  
16  
17  
18  
19  
20  
21  
22  
23  
24  
25  
26  
27  
28  
29  
30  
31  
32  
33  
34  
35  
36  
37  
38  
39  
40  
41  
42  
43  
44  
45  
46  
47  
48  
49  
50  
51  
52  
53  
54  
55  
56  
57  
58  
59  
60

$\ln(h_{\text{final}}/h_{\text{initial}})$ ) of 2.3 (or 90% thickness reduction). The width of the channel was 7mm. Samples were protected by three PTFE films in order to limit friction during deformation. This procedure was repeated between each deformation step of ~30% thickness reduction. At strains of about 1.4, the sheared extremities were removed with a diamond wire saw.

Each deformed crystal was sectioned, using a fine diamond wire saw, into small samples of a few mm. section which were electropolished and then annealed in a salt bath at temperatures of 245, 264, 306 or 322°C.

Vickers microhardness measurements were made on the RD-ND longitudinal section using a MXT microhardness tester and 25g loads (indents with diameters of 25-30 $\mu\text{m}$ ).

High resolution X-ray peak profiles were measured on the Goss and Brass oriented crystals using a PANalytical MRD diffractometer in high-resolution triple-axis mode. The incident beam of a sealed copper tube was monochromatized by a parabolic X-ray mirror coupled to a four-bounce Bartels monochromator preset for Cu-K $\alpha_1$  radiation. The diffracted beam was measured using a sealed proportional counter attached to an analyzer crystal with an angular acceptance of 12 arc seconds. This high resolution setup with negligible instrumental broadening (i.e. negligible optical aberration of the diffractometer) is necessary for the evaluation method based on the asymptotic behaviour of the intensity distribution [13]. The expected dislocation density in the recovered state is of the order of  $10^{13} \text{ m}^{-2}$ , which is just above the resolution of this evaluation technique [13]. For the analysis 220 peak profiles were measured in the  $\langle 110 \rangle$  normal direction of the Goss and Brass oriented samples. Evaluation of the average dislocation density and the average coherent domain size was done according to the momentum method [13, 14], based on the asymptotic behavior of the second and fourth-order restricted moments of the intensity distribution at large distance  $q = 2(\sin \theta - \sin \theta_0) / \lambda$  from the centre of the peaks. It is known that at large  $q$  values the asymptotic behavior of the moments depends only on the size and shape of the coherent diffraction domain [15] as well as the displacement field of the dislocations [16]. **The coherent diffraction domain size is a standard parameter determined from X-ray diffraction peak profiles. It can be linked to the dislocation cell size in cellular dislocation structure, but is usually smaller than the cell size since it is also sensitive to free dislocations in the cell interior.** The asymmetry of the line profiles, related to polarization of the dislocation structure and local internal stresses, [17] was also evaluated. Following Groma [16] the polarization of the dislocation structure can be characterized in terms of the parameter  $\langle s^{(2)} \rangle$ , describing the integral average value of the product between the sign dislocation density and the local

1  
2  
3 deformation gradient. Its value can be calculated from the 3<sup>rd</sup> order restricted moment of the  
4 intensity distribution (eq. (68) of [16]).  
5  
6  
7

8  
9 The EBSD analyses of the deformation substructures were made on the samples with a FEG-  
10 SEM (Zeiss Supra 55VP) using a step size of 0.05 to 0.15 $\mu$ m (accelerating voltage 20 kV,  
11 working distance 15 mm). Crystalline orientations were determined through Kikuchi patterns  
12 recorded by a high speed digital camera using the HKL Channel 5 software. EBSD mappings  
13 were analyzed either by standard software or by in-house programs using the orientation  
14 library Orilib2, based on the quaternion representations of crystal rotations. It was convenient  
15 to visualize the substructure using both standard band contrast images and local rotation axis  
16 images. As shown by Albou et al [18] the local rotation axes  $\underline{r}$  can be imaged using a colour  
17 convention such that the three primary colours (Red, Blue, Green = RGB) are associated with  
18 the three components of  $\underline{r}$  in the rolling frame (RD, TD, ND). Each pixel of the map then has  
19 a well defined colour directly linked to the disorientation axis.  
20  
21  
22  
23  
24  
25  
26  
27  
28  
29

### 30 3. Results

#### 31 3.1 Mechanical properties

32  
33 The channel-die compression stress-strain curves of the single crystals and a reference  
34 polycrystal are plotted in Fig 1. The reference polycrystal possessed a weak texture ( $f_{\max} =$   
35 2.6, as characterized by EBSD measurements on 5000 grains). The discontinuities on the  
36 curves correspond to the small stress variations on unloading, lubrication and reloading the  
37 sample; the true stress-strain curves can be derived from the resulting envelope. Clearly the  
38 flow stresses increase from the lowest (Bs) through Goss and S to the polycrystal. This  
39 roughly fits with the Taylor factors calculated for the boundary conditions of channel-die  
40 compression of single crystals, i.e.  $\sqrt{6}$  for Bs and Goss and 3.12 for S. A standard full  
41 constraints value of 3.31 can be taken for plane strain compression of a non-textured  
42 polycrystal. The distinctive work hardening rate of the Goss orientation, above that of  
43 orientations with the same Taylor factor, has already been noted previously [19]  
44  
45  
46  
47  
48  
49  
50  
51  
52

53 Figure 1 near here  
54  
55  
56

57 The crystals start deforming at an initial flow stress  $\sigma_0$  about 15 MPa then work harden  
58 up to flow stresses of 80-100MPa at strains of 2.3 (well into stage IV hardening). An  
59 elementary estimate of the final dislocation density using the standard square root law:  
60

$$\sigma - \sigma_0 = M\alpha\mu b\sqrt{\rho} \quad (M= 2.45, \alpha=0.3, \mu=26 \text{ GPa}, b = 2.86 \text{ m}^{-10})$$

and taking  $\sigma - \sigma_0 = 80 \text{ MPa}$  for the Goss crystal gives a dislocation density at  $\varepsilon=2.3$  of about  $2 (\pm 0.6) \times 10^{14} \text{ m}^{-2}$ . The Vickers microhardness values of the as-deformed crystals are in line with the compressive flow stresses, i.e.  $39 \pm 0.2 \text{ Hv}$ ,  $43.5 \pm 0.3 \text{ Hv}$  and  $44.9 \pm 0.8 \text{ Hv}$  for the Bs, Goss and S orientations respectively. Note that the initial, un-deformed values are quite similar:  $20.1 \pm 0.1 \text{ Hv}$ ,  $20.2 \pm 0.1 \text{ Hv}$  and  $19.3 \pm 0.3 \text{ Hv}$  for Bs, Goss and S respectively.

The variations of the microhardness with (log) annealing time are given in Figure 2 for the 3 orientations respectively a) Bs, b) Goss and c) S. The first point is that they fit a logarithmic time dependency quite well over the 4 time decades examined here. The second point is that, for any orientation, the linear hardness (log t) plots are decreased to lower Hv at higher temperatures but the slopes are not very dependent on temperature. It seems that, to first order, the temperature only influences the very first part of the annealing or recovery stages (less than 10 secs) but thereafter does not play a major role, at least in this range.

Figure 2 near here

Finally and this is the most important result, there is a clear difference between the rate of hardness decrease of the Bs orientation compared with the other two: the slopes of the Goss and S plots are about twice those of the Bs orientation. This difference of recovery rates is brought out more clearly in the plots of the fractional residual hardening  $R_{Hv}$  vs log time for the three temperatures (Figure 3). Here  $R_{Hv} = \frac{Hv - Hv_0}{Hv_\varepsilon - Hv_0}$  where  $Hv_0$  and  $Hv_\varepsilon$  are the hardness values in the un-deformed and as-deformed states respectively.

Figure 3 near here

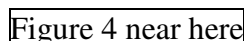
The figures show clearly that the Bs orientation has a recovery slope about half that of the other two (which cannot really be separated, except possibly at long times when the Goss recovery rate appears somewhat faster). The Bs orientation starts off with a much lower hardness than the others but after  $10^5$  s recovery its hardness is equivalent to that of S or greater than that of Goss. Note that for all orientations the amount of recovery is quite large,  $R_{Hv}$  decreasing to 0.5 or 50% recovery at the longer times. The logarithmic time law means that, for the Brass orientation, the times to a given  $R_{Hv}$  can be at least 2 orders of magnitude greater than those of the other two orientations.



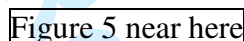
1  
2  
3 In fact it turns out that the recovery rates of the Goss and S crystals are comparable to those of  
4 cold rolled ( $\epsilon=3$ ) commercial purity Al as published by Furu et al [20]. Compared with the  
5 recovery rates of the latter, at about the same temperatures, the somewhat slower hardness  
6 recovery in the Al-Mn crystals can be linked to the lower initial deformation of 2.3.  
7  
8  
9

### 10 11 12 3.2 X-ray line profile analysis

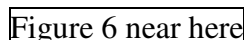
13 As described in the section on experimental procedures, the diffraction profiles of the 220  
14 lines have been measured for the Bs and Goss orientations as a function of recovery annealing  
15 time at 246°C and 264°C.  
16  
17  
18

19  Figure 4 near here

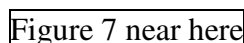
20  
21  
22  
23 Figure 4 plots the normalized intensity ratios as a function of the profile width parameter  $q$  for  
24 the Bs (a) and Goss (b) orientations. They both show a rapid decrease of the extent of line  
25 broadening with time, even after times of only 10 seconds. The corresponding dislocation  
26 densities derived from the 2<sup>nd</sup> and 4<sup>th</sup> order moments of the intensity distributions are given in  
27 Fig.5 (a) for Bs and (b) for Goss.  
28  
29  
30

31  Figure 5 near here

32  
33  
34  
35 First they give an initial as-deformed dislocation density of  $2 \cdot 10^{14} \text{ m}^{-2}$  which is the value  
36 expected from the final flow stresses. Secondly, there are very rapid and major variations of  
37 the dislocation densities during the primary stages of recovery. In the case of the Bs  
38 orientation the dislocation density decreases fairly progressively by a factor of up to 4 after 10  
39 mins. In the case of the Goss orientation the dislocation density decreases almost immediately  
40 to about  $5 \cdot 10^{13} \text{ m}^{-2}$  after 10 seconds and then only slowly thereafter for times up to 1 hour.  
41  
42  
43  
44  
45

46  Figure 6 near here

47  
48  
49  
50 Figure 6 illustrates the variation of coherent domain size with time during these anneals, a) for  
51 the Bs and b) for the Goss orientations respectively. Here again the Goss orientation exhibits a  
52 significant evolution, increasing from about 200 nm to 700 nm while the Bs orientation  
53 reveals only a marginal increase. As often, the coherent domain sizes tend to be smaller than  
54 the cell size as measured by EBSD (see following section) but their evolution is quite  
55 consistent with the hardness variations.  
56  
57  
58  
59  
60

 Figure 7 near here

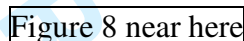
1  
2  
3 The X ray line profile analyses of the deformed Brass and Goss crystals also highlight a subtle  
4 feature of the square root hardening law. According to Fig. 7 the 220 peaks of both as-  
5 deformed crystals coincide, which could be considered rather surprising since the  
6 corresponding stress-strain curves (Fig. 1) are different; one would expect different  
7 dislocation densities for the two orientations. Due to the anisotropic displacement field of  
8 dislocations, it is known [16] that peak broadening depends on the diffraction vector and its  
9 relative orientation with the dislocations [21]. The contrast factor  $C$  for the 220 reflection has  
10 been calculated using the freely available ANIZC software [21, 22] assuming that it is mainly  
11 the active slip systems that are populated: two systems ( $a_2$  and  $b_1$ ) for the Brass crystal [18]  
12 and four systems ( $a_1$ ,  $a_2$ ,  $b_1$  and  $b_2$ ) for the Goss crystal [19]. The influence of these  
13 dislocation types on the contrast factor has been studied. For the dislocation density  
14 evaluations an equal proportion of screw, edge and mixed ( $30^\circ$  and  $60^\circ$ ) dislocations was  
15 assumed giving a contrast factor of  $C = 0.2015$  for both crystals. The equal 220 contrast  
16 factors for the Brass and Goss crystals as well as the identical intensity distributions (Fig. 7)  
17 imply that the dislocation density is necessarily the same in the deformed state of both  
18 crystals. Their different flow stresses (Fig. 1) should therefore be interpreted as a consequence  
19 of their specific dislocation interactions giving different  $\alpha$  values. The higher number of  
20 activated slip systems in the Goss crystal compared to Brass (four and two, respectively)  
21 suggests that  $\alpha$  is higher for the Goss orientation in agreement with the flow stresses. Further  
22 work is currently under way for an accurate evaluation of  $\alpha$ .

23  
24  
25  
26  
27  
28  
29  
30  
31  
32  
33  
34  
35  
36  
37  
38  
39 Another remarkable feature of the diffraction profiles is the asymmetry of the peaks  
40 characterizing the deformed state. As shown by Figs. 4 and 7 their maximum is shifted to the  
41 left compared to peaks of the annealed crystals. This is in agreement with the composite  
42 model of heterogeneous dislocation distributions [17] and indicates the presence of long range  
43 compressive internal stresses in the hard dislocation-rich cell walls. In the composite model  
44 [17] such stresses are associated with interface dislocations corresponding to a polarized  
45 distribution of edge dislocation segments. The sign of the asymmetry of the 220 and 002  
46 profiles (not shown here) also corresponds qualitatively to the prediction of the composite  
47 model, indicating the existence in dislocation walls of compressive strains in the direction of  
48 the applied external stress (ND) and tensile strains along RD. The residual strains, however,  
49 have not been evaluated since no unequivocal decomposition of the asymmetric peaks exists  
50 (unless an extra condition on Poisson's ratio determined from 220 and 002 peaks is imposed  
51 [17]). Therefore the asymmetry has been characterized based on the 3<sup>rd</sup> order restricted  
52 momentum of the intensity distribution in terms of the dislocation polarization parameter  
53  
54  
55  
56  
57  
58  
59  
60

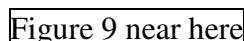
1  
2  
3  
4  $\langle s^2 \rangle$  according to the general peak broadening model of Groma [16, 23]. This polarization  
5  
6 parameter, characterizing peak asymmetry, is about  $4 \cdot 10^{21} \text{ m}^{-3}$  in the as-deformed state and  
7  
8 decreases rapidly by about two orders of magnitude (to about  $10^{19} \text{ m}^{-3}$ ) after the first 10 sec of  
9  
10 annealing.

### 11 12 13 **3.3 EBSD microstructure evolution.**

14  
15 Figure 8 gives an overview of the substructure evolution at  $264^\circ\text{C}$  of the 3 crystals from the  
16  
17 as-deformed state to the recovered structure after 34h. The immediate impression is that the  
18  
19 rather complex substructure of the Bs orientation varies very little, whereas the Goss and S  
20  
21 orientations develop equiaxed subgrains after about 1hour, or even before. The well  
22  
23 developed and coarsened subgrain structure of the Goss orientation after 34h is quite obvious,  
24  
25 although there is no sign of discontinuous or abnormal subgrain growth. This is in contrast to  
26  
27 the observations of Ferry and Humphreys [24] on channel-die compressed Goss crystals  
28  
29 ( $0.7 < \epsilon < 3$ ) of Al-0.05 at% Si who found abnormal subgrain growth at annealing temperatures  
30  
31 above  $250^\circ\text{C}$ . The reasons for this discrepancy are unknown at the moment.

32  
33  
34  
35  
36  
37  
38  
39  
40  
41  
42  
43  
44  
45  
46  
47  
48  
49  
50  
51  
52  
53  
54  
55  
56  
57  
58  
59  
60  


From the pole figures of Figure 8 it is apparent that the orientation spreads after deformation  
are very dependent on the crystal orientation. It is therefore important to examine the  
disorientation distributions and these are shown in Fig 9 for all the crystal orientations both  
as-deformed and after annealing 10mins at  $320^\circ\text{C}$  (disorientation frequency distributions with  
respect to the average orientation). The deformed Bs orientation is characterized by very low  
disorientations with a spread of 1 to  $6^\circ$ . On the other hand both the Goss and S orientations  
exhibit quite large disorientations with spreads up to  $18^\circ$  and averages of 6 and  $5.5^\circ$   
respectively. Another metric for the disorientation is the average non-correlated disorientation  
which represents the average disorientation between pairs of pixels chosen at random from the  
EBSD map [25]. Table 1 gives the values for the as-deformed and annealed states and it can  
be seen that, initially, the non-correlated disorientations are close to  $3.7^\circ$  for Bs but  $8^\circ$  for  
Goss and S.



A detailed description of the formation of the deformation microstructure of the Bs orientation  
has been given in [18] and more details of the Goss and S structures will be published [26].  
The other distinctive feature is the rotation axes associated with these disorientations. The Bs

1  
2  
3 crystal possesses rotation axes mostly about TD [18] while the rotations in the Goss crystal  
4 are mainly around ND (Figure 8). The S orientation, however, is characterized by a near  
5 random distribution of rotation axes as seen in the pole figure of Fig. 8. After annealing  
6 10mins at 320°C there are minor changes in the disorientation distributions which mostly  
7 concern the Goss orientation whose spread at both high and low angles tends to decrease. Its  
8 non-correlated average disorientation also decreases from 8.6 to near 7°.

9  
10 Figs 10-12 illustrate in more detail the typical microstructure and microtexture changes of the  
11 3 crystals from the as-deformed to the well-recovered state (34h at 264°C corresponding to  
12  $R_{Hv}$  about 0.5). The Bs orientation of Figure 10 confirms that there is very little substructure  
13 evolution in this orientation: the subgrain size, morphology and orientation distribution are  
14 effectively unchanged (although both the hardness and the dislocation density have decreased  
15 substantially).

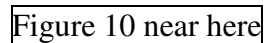
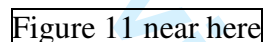
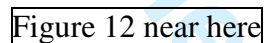
16  
17  
18  
19  
20  
21  
22  
23  
24  
25  
26  
27  
28  
29  
30  
31  
32  
33  
34  
35  
36  
37  
38  
39  
40  
41  
42  
43  
44  
45  
46  
47  
48  
49  
50  
51  
52  
53  
54  
55  
56  
57  
58  
59  
60  


Figure 11 demonstrates a clear evolution of the Goss substructure; the subgrains are closed up  
(i.e. the misorientated boundary segments of  $<1^\circ$  disappear), grow substantially from about  
less than 1 $\mu\text{m}$  to nearly 3 $\mu\text{m}$  and also become more equiaxed. This is quite similar to the  
annealing behaviour of the S orientation (Figure 12).





#### 4. Discussion

To our knowledge this is the first systematic study of recovery in strongly deformed single  
crystals and is also the first to apply different characterisation techniques (hardness, X-ray  
line profile analysis and EBSD orientation mapping) to the problem. These techniques  
characterise the material at different length scales, very roughly as follows; X-rays at the nm,  
EBSD at 100nm and the micro hardness at the  $\mu\text{m}$  scale. The micro hardness values are  
probably the most difficult to justify in relation to the physical mechanisms of recovery since  
they include contributions from the dislocation substructure hardening in the material (under  
study) plus that generated during the microhardness test by the plastic strain around the  
indenter. The latter could be orientation dependent, but since the compression stress-strain  
curves are not very different it appears reasonable to assume that the work hardening due to  
the indenter should be similar for the 3 orientations. The fractional residual hardening should

1  
2  
3 therefore be a reasonable guide to the basic orientation dependency of recovery in the present  
4 case. It certainly reveals the same general tendencies, namely that the Goss and S orientation  
5 recover much quicker than the Bs orientation. Flow stresses and hardness of cell-forming  
6 metals are often modelled using two parameters: the dislocation density and the cell size.  
7 Since the average dislocation densities are almost identical for the two orientations (Figs 5a  
8 and 5b) it is reasonable to link the recovery of hardness to changes in the dislocation cell/sub-  
9 grain size, which is obtained from peak-profile analysis through the parameter called  
10 “coherent domain size”. Figs. 6a and 6b show that sub-grain coarsening takes place much  
11 faster in the Goss oriented crystal in good qualitative agreement with hardness observations.  
12 Thus after long term recovery at 264°C the hardness values of the 3 crystals are 32 for Bs and  
13 S but only 29 for Goss, in qualitative agreement with the coherent domain sizes of 700 nm for  
14 Goss and 300 nm for Bs. This result suggests that mechanical strength of recovered states is  
15 primarily determined by the underlying sub-grain structure as proposed earlier by Tabata et al.  
16 [27].

17  
18 In all cases the overall rate-controlling mechanism in this Al-0.05 at. % Mn alloy is expected  
19 to be dislocation annihilation by solute diffusion-controlled climb of dislocations in the local  
20 stress fields, according to the Nes model [28]. Thus it has been shown by Barou et al [12] that,  
21 for similarly deformed Al-Mn polycrystals recovered over a wider temperature range of 150-  
22 300°C, the activation energy can be taken as that of solute diffusion minus a term for the  
23 driving force for stress-assisted dislocation climb (following the basic formulation of  
24 Kuhlmann et al [8] and summarised in [29, 30]). In the work of Barou [11] it was also  
25 observed that the Goss oriented grains tended to have a sub-grain growth rate about twice that  
26 of the other grains (although a rapid recovery of the S oriented grain was not detected in the  
27 deformed polycrystals).

28  
29 In principle this orientation dependency of recovery can be attributed to differences in either  
30 driving force (e.g. dislocation density) or defect mobilities. In the present case there are only  
31 minor differences in the driving forces, as measured by dislocation densities (and flow  
32 stresses), so to first order they can be taken to be roughly constant. We therefore consider that  
33 the recovery rates here are essentially influenced by the mobilities of the defects (dislocations  
34 or dislocation boundaries) in the local orientation gradients of the deformed crystals. We  
35 recall that plane strain compression of the brass orientation only develops small  
36 misorientations of about 3-4° whereas the S and Goss crystals develop misorientations  
37 roughly twice as high (Figure 9).

1  
2  
3 For the later stage of recovery by sub-grain growth, the misorientations of low-angle  
4 boundaries are known to have a pronounced effect on boundary mobility. Humphreys [31] has  
5 proposed an empirical exponential misorientation ( $\bar{\theta}$ ) dependency of LAGB mobilities of the  
6 form  
7  
8  
9

$$M = M_b \left[ 1 - \exp \left\{ -B \left( \frac{\bar{\theta}}{\theta_b} \right)^A \right\} \right] \quad (1)$$

10 where  $M_b$  is the mobility of a high angle grain boundary of misorientation  $\theta_b \sim 15^\circ$ .

11 This mobility expression has been confirmed by measurements from the same group of sub-  
12 grain growth in initial Goss [32] and cube [6] oriented Al-0.05at.%Si crystals. From their  
13 results for the average misorientations one expects the sub-boundary mobilities in the Goss  
14 and S crystals to be at least an order of magnitude greater than those of the Bs orientation with  
15 significant effects on the sub-grain coarsening rates. This process is currently being validated  
16 by vertex simulations of sub-grain coarsening in Al grains containing orientation gradients  
17 [33] and preliminary results do indicate a major influence of local misorientations. Clearly,  
18 the later stages of recovery by sub-grain growth as seen in Figure 8 will be strongly  
19 influenced by the misorientation distributions.  
20  
21  
22  
23  
24  
25  
26  
27  
28  
29  
30  
31

32 The results of Xing et al [7] indicating higher recovery rates in unstable grain orientations  
33 after cold rolling of Al polycrystals can be qualitatively interpreted in the same manner; in  
34 general (though not always) unstable grains tend to develop higher misorientations than stable  
35 grains.  
36  
37  
38

39 The first stages of recovery, before sub-grain growth, reveal less orientation effects. X-ray  
40 peak broadening measurements indicate a very rapid initial decrease of the initial dislocation  
41 density for both orientations. The dislocation densities decrease by factors of about 3 within  
42 about 10 seconds at 264°C (0.57 Tm) and only slowly thereafter. The first stage of recovery in  
43 cell structures is considered to be the annihilation of dislocation dipoles (those that do not  
44 contribute to the cell misorientation) by thermally activated climb within or near the cell  
45 walls. This view is supported by the present line profile analysis showing that the deformed  
46 state is characterized by strongly asymmetrical X-ray diffraction peaks. This anti-symmetry  
47 decreases by about two orders of magnitude after the first 10 sec of annealing indicating the  
48 disappearance of long range internal stresses and of dislocation dipoles considered as their  
49 sources. This means that the early stage of recovery is related to annihilation of dislocation  
50 dipoles and/or dislocation walls with dipolar character. Since the misorientation distribution  
51  
52  
53  
54  
55  
56  
57  
58  
59  
60

1  
2  
3 hardly changes during this process, sub-grain boundaries made up by dislocations of the same  
4 sign are not affected.

5  
6 Bailey and Hirsch [34] first reported a relatively rapid stored energy decrease due to recovery  
7 in deformed Ag as measured by calorimetry (between 15 and 60 mins. at homologous  
8 temperatures near 0.4T<sub>m</sub>). Their TEM investigations did not detect a significant decrease of  
9 the dislocation density but work by Young et al [35] on high purity Al suggested that the first  
10 stages of recovery were due to annealing out of small dislocation loops and straightening of  
11 dislocations so reducing their overall density (albeit without quantitative analysis).  
12

13  
14 The early stages of recovery appear to be more sensitive to temperature. For example, after 10  
15 seconds annealing the microhardness values of all 3 orientations are significantly lower at the  
16 higher temperatures (Fig 2) – and this may be linked to the dislocation annihilation  
17 mechanisms. The overall hardness recovery rates can be described by a law of the form  
18

$$R_{HV} = 1 - C \cdot \ln(1 + t/\tau) \quad (2)$$

19  
20 where the  $\tau$  term includes the initial temperature dependency of the process. The later stages,  
21 however, are less temperature dependent and this agrees qualitatively with the hardness  
22 variations of rolled commercial purity aluminium described by Furu et al. [20].  
23

24  
25 There are also implications for recrystallization nucleation; in rolled fcc metals it is well  
26 known that cube nuclei usually develop first as a result of rapid recovery in cube grains  
27 (Ridha and Hutchinson [5]). Cube grains were not investigated in this work for practical  
28 reasons since they break up during large strain cold rolling into fragments of a few microns  
29 which preclude the type of measurements made here. We consider that if cube grain recovery  
30 had been measured in the same way it would be faster than the deformed Goss crystals.  
31 However, it is also known that other common recrystallization components in fcc metals and  
32 alloys are Goss and S. It is therefore reasonable to suggest that their relatively fast recovery  
33 rates enable these orientations to develop micron-sized sub-grains that then become  
34 recrystallization nuclei before other orientations (apart from cube) can develop.  
35  
36  
37  
38  
39  
40  
41  
42  
43  
44  
45  
46  
47  
48  
49  
50

## 51 52 **5. Summary and Conclusions**

53  
54 A static recovery analysis has been carried out on strongly deformed Al single crystals with  
55 the aim of characterizing the orientation dependency of the process. The single crystal  
56 orientations (Brass, Goss and S) are relatively stable in plane strain compression so develop  
57 relatively homogeneous deformation microstructures after 90% thickness reduction but with  
58 significant differences in misorientation distributions. The recovery kinetics, up to about 50%  
59  
60

1  
2  
3 recovery, are described by microhardness variations and the mechanisms investigated by X  
4 ray line broadening analysis and FEG-SEM EBSD orientation mapping. A standard  
5 logarithmic time dependency is obtained for the microhardness variations of all crystals. It is  
6 shown that the microhardness recovery rates of the Brass oriented crystals are systematically  
7 lower than those of the other two orientations by a factor of about 2 over the time period  
8 investigated here. The X-ray line profile analysis shows that the dislocation densities decrease  
9 rapidly in the first stages of recovery (<1 min) by dislocation dipole annihilation, and then  
10 more slowly thereafter. In the Goss and S orientations the later stage of recovery is due to  
11 sub-grain growth as characterized by EBSD orientation mapping. The orientation dependency  
12 is ascribed to the relatively low misorientations developed by plastic straining in the Brass  
13 crystals (average about 4°) compared with the Goss and S orientations (about 7-8°). The  
14 microhardness and microstructure evolution results are discussed in terms of the different  
15 mechanisms controlling recovery over 4 time decades and, in particular, the importance of  
16 defect mobility in deformation-induced orientation gradients.  
17  
18  
19  
20  
21  
22  
23  
24  
25  
26  
27  
28  
29

### 30 **Acknowledgements**

31 The authors wish to thank the Indo-French Centre for the Promotion of Advanced Research  
32 (IFCPAR) for the provision of a grant to facilitate a cooperative project on orientation  
33 dependent recovery with the group of Professor Indra Samajdar in the Metallurgical  
34 Engineering and Materials Science Department of IIT Bombay.  
35  
36  
37  
38  
39

### 40 **References**

- 41  
42 [1] W.F. Hosford, Acta Metall., 14 (1966) p1085.  
43  
44 [2] J. H. Driver, D. Juul Jensen and N. Hansen, Acta Metall. Mater., 42 (1994) p3105.  
45  
46 [3] G Winther, X Huang and N Hansen, Acta Mater. 48 (2001) p2187.  
47  
48 [4] X Huang and G. Winther, Phil Mag. 87 (2007) p5189.  
49  
50 [5] A.A. Ridha and W.B. Hutchinson, Acta Metall. 30 (1982) p1929.  
51  
52 [6] Y. Huang, F.J. Humphreys and M. Ferry, Acta Mater. 48 (2000) p2543.  
53  
54 [7] Q. Xing, X. Huang and N. Hansen, Metall. and Mater. Trans. 37A (2006) p1311.  
55  
56 [8] D. Kuhlmann, G. Masing and J. Raffelseiper, Zeits. für Metallk. 40 (1949) p241.  
57  
58 [9] T. Hasegawa and U. F. Kocks, Acta Metall. 27 (1979) p1705.  
59  
60 [10] A. Godfrey, D. Juul Jensen and N. Hansen, Acta Mater. 49 (2001) p2429.  
[11] F Barou, C Maurice, J-M Feppon and J H Driver, Int. J. Mater.Res. 4 (2009) p516.



- 1  
2  
3 [12] F Barou, C Maurice, J-M Feppon and J H Driver, Proc Rex and GG 4 (2010) to be  
4 published  
5  
6 [13] A. Borbély and I. Groma, I., Appl. Phys. Lett. 79 (2001) p1772.  
7  
8 [14] A. Borbély, A. Révész and I. Groma, Z. Kristallogr. Suppl. 23 (2006) p87.  
9  
10 [15] A. J. C. Wilson, Proc. Phys. Soc. 80 (1962) p286.  
11  
12 [16] I. Groma, Phys. Rev. B 57, (1998) p7535.  
13  
14 [17] H. Mughrabi, T. Ungár, W. Kienle, M. Wilkens, Phil. Mag. A 53 (1986) 793.  
15  
16 [18] A. Albou, C Maurice and J H Driver, Acta Mater. 58 (2010) p3022.  
17  
18 [19] F Basson and J H Driver Acta Mater. 48 (2000) p2101.  
19  
20 [20] T. Furu, R. Orsund and E. Nes, Acta Metall. Mater. 43 (1995) p2209.  
21  
22 [21] A. Borbély, J. Dragomir-Cernatescu, G. Ribárik, and T. Ungár, J. Appl. Cryst. 36 (2003)  
23 p160.  
24  
25 [22] <http://metal.elte.hu/anizc/>  
26  
27 [23] I. Groma and G. Monnet, J. Appl. Cryst. 35 (2002) p589.  
28  
29 [24] M Ferry and F J Humphreys, Acta Metall Mater 44 (1996) p1293.  
30  
31 [25] A. Borbély, Cl. Maurice, D. Piot, J.H. Driver, Acta Mater. 55 (2007) p487.  
32  
33 [26] A. Albou, C Maurice and J H Driver to be published  
34  
35 [27] T Tabata, H Fugita, M-A Hiraoka, S Miyake, Phil. Mag. 46 (1982) p801.  
36  
37 [28] E Nes, Acta Metall. Mater. 43 (1995) p2189.  
38  
39 [29] D Kuhlmann-Wilsdorf, Phil. Mag. A 79 (1999) p955.  
40  
41 [30] D Kuhlmann-Wilsdorf, Mater. Sci. Forum, vols 331-337 (2000) p689.  
42  
43 [31] FJ Humphreys, Acta Mater. 45 (1997), p 4231.  
44  
45 [32] Y Huang and FJ Humphreys, Acta Mater. 48 (2000) p2017.  
46  
47 [33] A Majumdar, C Maurice, J H Driver, Proceedings ICOTOM 16, to be published.  
48  
49 [34] J E Bailey and PB Hirsch, Phil Mag 5 (1960) p485.  
50  
51 [35] C T Young, T J Headley and J L Lytton, Mater Sci Eng. 81 (1986) p 391.  
52  
53  
54  
55  
56  
57  
58  
59  
60

Table 1 Average non-correlated disorientations from EBSD maps

Orientation	As-deformed $\varepsilon=2.3$	Recovered 10min at 320°C
Bs	3.7°	3.6°
Goss	8.5°	6.8°
S	7.8°	8.2°

For Peer Review Only

## Figure captions

Figure 1. True stress-strain curves of Al-0.1%Mn single and polycrystals.

Figure 2. Vickers microhardness values of the 3 single crystal orientations during recovery annealing at different temperatures. The error bar on Figure 2c (S orientation) is the largest measured error due to some local heterogeneities; the errors on the others are less than or equal to the size of the symbols.

Figure 3. Fractional residual microhardness values of the crystals during recovery annealing at 3 temperatures.

Figure 4. Normalized X ray intensity ratios as a function of the 220 profile width parameter  $q$  for (a) the Bs and (b) the Goss orientations, both as-deformed and after recovery annealing at 264°C.

Figure 5. Dislocation density evolution during annealing of Bs and Goss deformed crystals

Figure 6. Evolution of the coherent domain size of the Bs and Goss crystals during recovery annealing.

Figure 7. Normalized X ray intensity ratios as a function of the 220 profile width parameter  $q$  for the Bs and Goss orientations, illustrating the peak asymmetry after deformation and its absence after recovery annealing at 246°C.

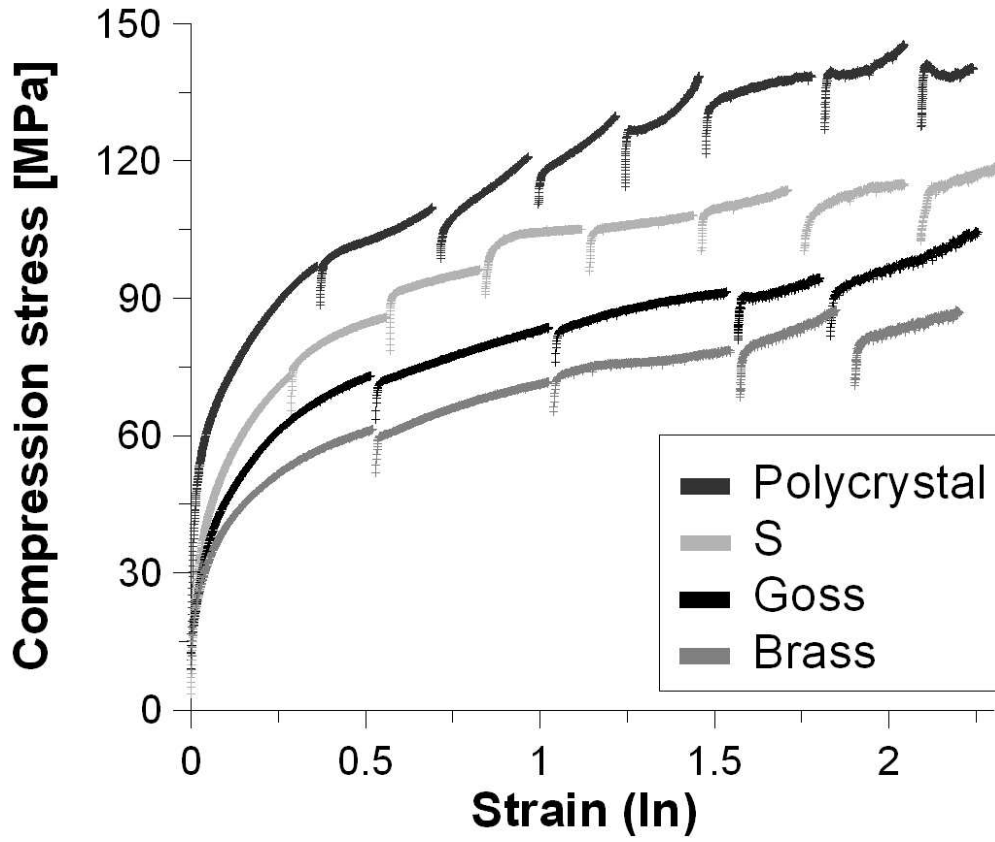
Figure 8. The evolution, during annealing at 264°C, of the deformation substructure of 3 crystal orientations from the as-deformed state to 34hs recovery. Band contrast images from EBSD orientation maps. The {111} pole figures in the as-deformed state are shown above the corresponding crystal microstructures.

Figure 9. The disorientation distributions of 3 crystal orientations as-deformed and after 10min. at 320°C (pixel orientation wrt the mean orientation: average values for the Bs, Goss and S crystals are 2.7, 6 and 5.5° respectively).

Figure 10. EBSD analysis of the Brass crystal by band contrast, disorientation axis maps and misorientation line scans (w. r. t. first point).

Figure 11. EBSD analysis of the Goss crystal by band contrast, disorientation axis maps and misorientation line scans (w. r. t. first point).

Figure 12. EBSD analysis of the S crystal by band contrast, disorientation axis maps and misorientation line scans (w. r. t. first point).

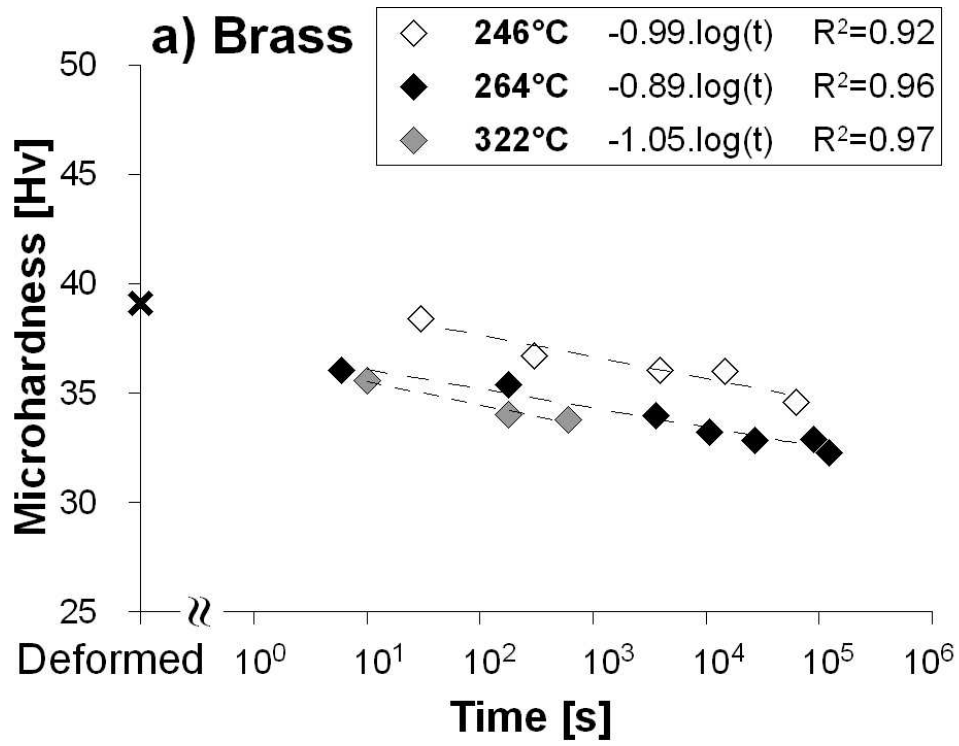


87x73mm (300 x 300 DPI)

Preview Only

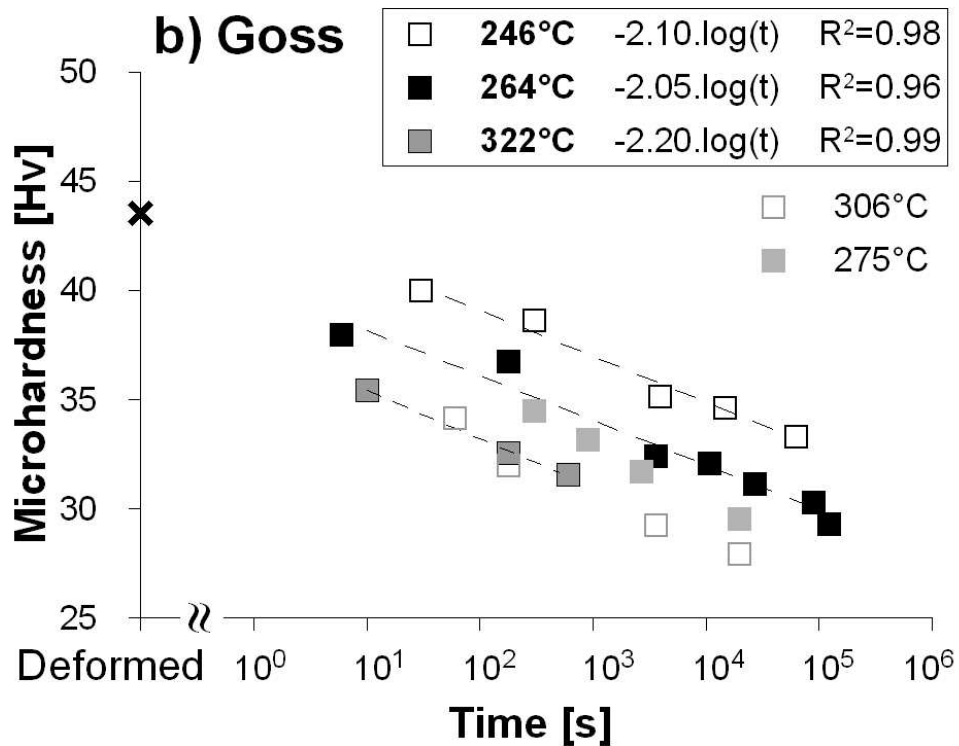
1  
2  
3  
4  
5  
6  
7  
8  
9  
10  
11  
12  
13  
14  
15  
16  
17  
18  
19  
20  
21  
22  
23  
24  
25  
26  
27  
28  
29  
30  
31  
32  
33  
34  
35  
36  
37  
38  
39  
40  
41  
42  
43  
44  
45  
46  
47  
48  
49  
50  
51  
52  
53  
54  
55  
56  
57  
58  
59  
60

1  
2  
3  
4  
5  
6  
7  
8  
9  
10  
11  
12  
13  
14  
15  
16  
17  
18  
19  
20  
21  
22  
23  
24  
25  
26  
27  
28  
29  
30  
31  
32  
33  
34  
35  
36  
37  
38  
39  
40  
41  
42  
43  
44  
45  
46  
47  
48  
49  
50  
51  
52  
53  
54  
55  
56  
57  
58  
59  
60

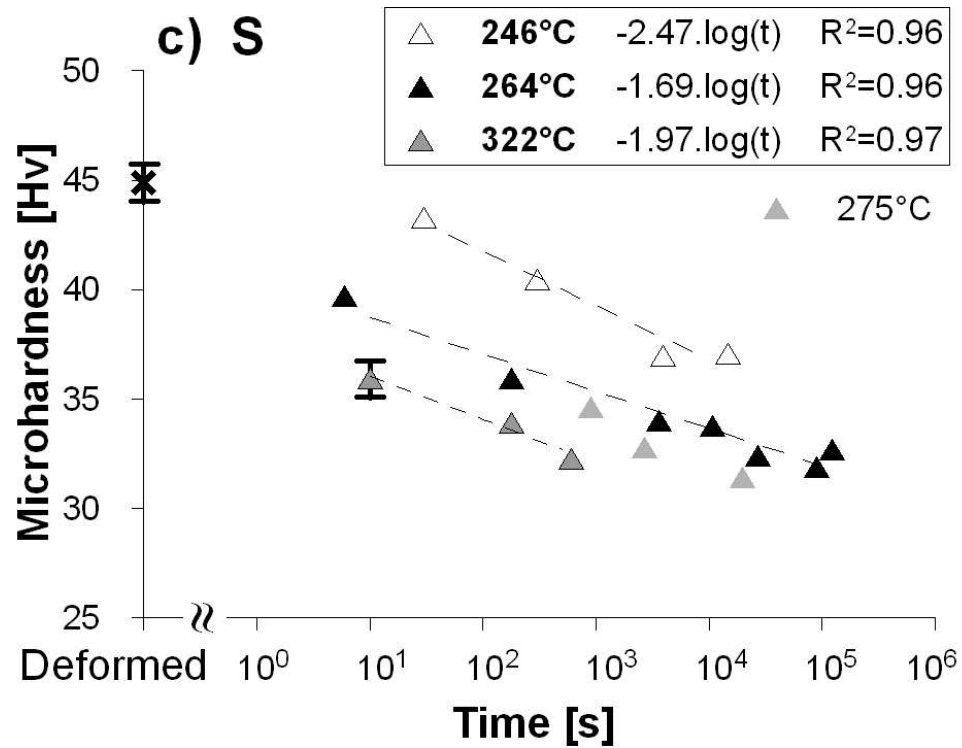


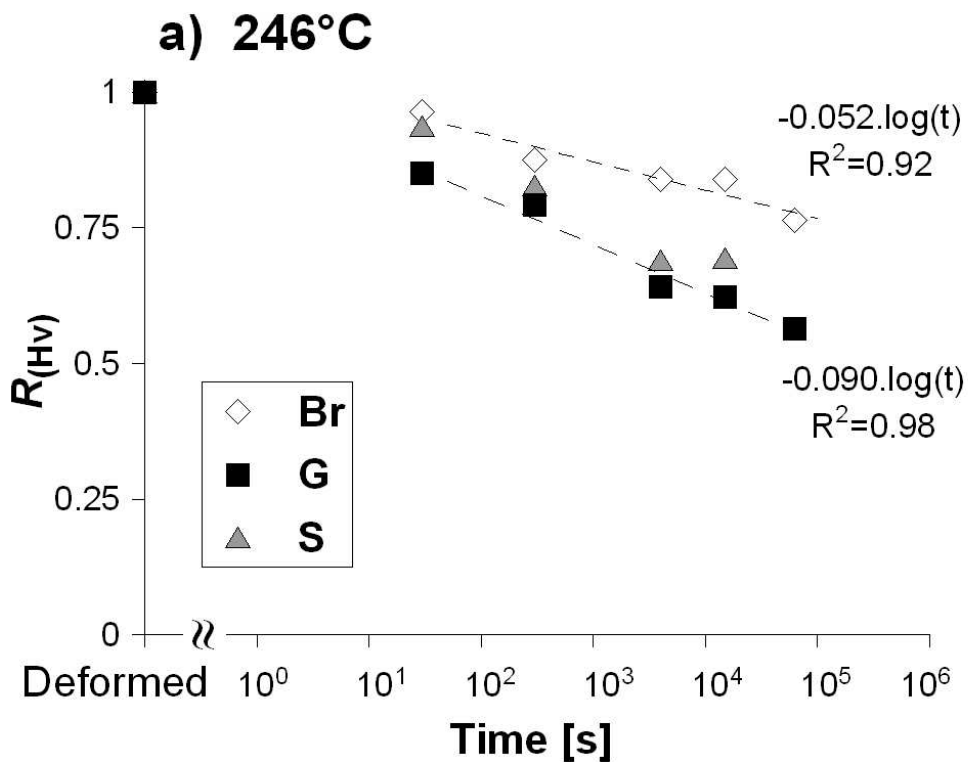
82x60mm (300 x 300 DPI)

View Only



82x60mm (300 x 300 DPI)





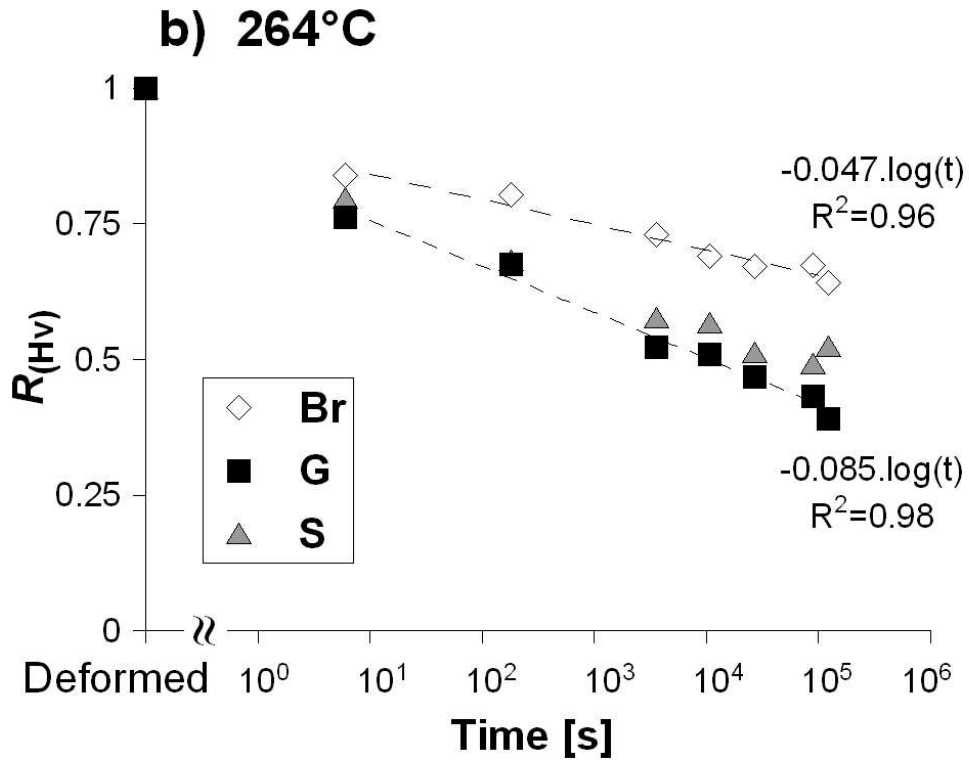
82x62mm (300 x 300 DPI)

new Only

1  
2  
3  
4  
5  
6  
7  
8  
9  
10  
11  
12  
13  
14  
15  
16  
17  
18  
19  
20  
21  
22  
23  
24  
25  
26  
27  
28  
29  
30  
31  
32  
33  
34  
35  
36  
37  
38  
39  
40  
41  
42  
43  
44  
45  
46  
47  
48  
49  
50  
51  
52  
53  
54  
55  
56  
57  
58  
59  
60

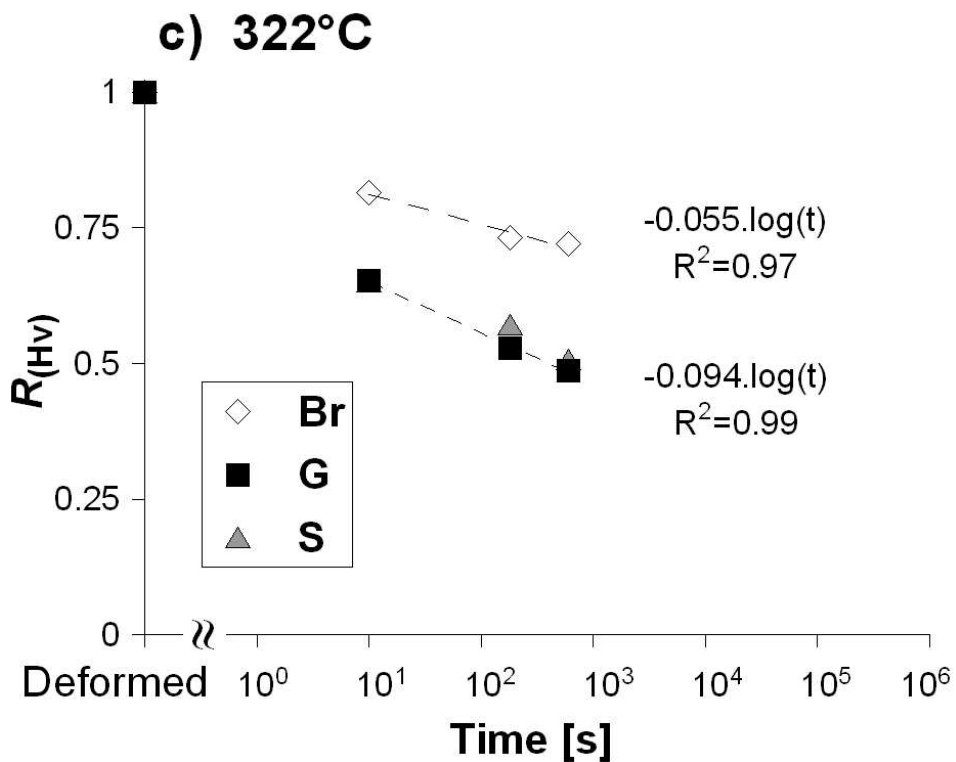


1  
2  
3  
4  
5  
6  
7  
8  
9  
10  
11  
12  
13  
14  
15  
16  
17  
18  
19  
20  
21  
22  
23  
24  
25  
26  
27  
28  
29  
30  
31  
32  
33  
34  
35  
36  
37  
38  
39  
40  
41  
42  
43  
44  
45  
46  
47  
48  
49  
50  
51  
52  
53  
54  
55  
56  
57  
58  
59  
60



82x62mm (300 x 300 DPI)

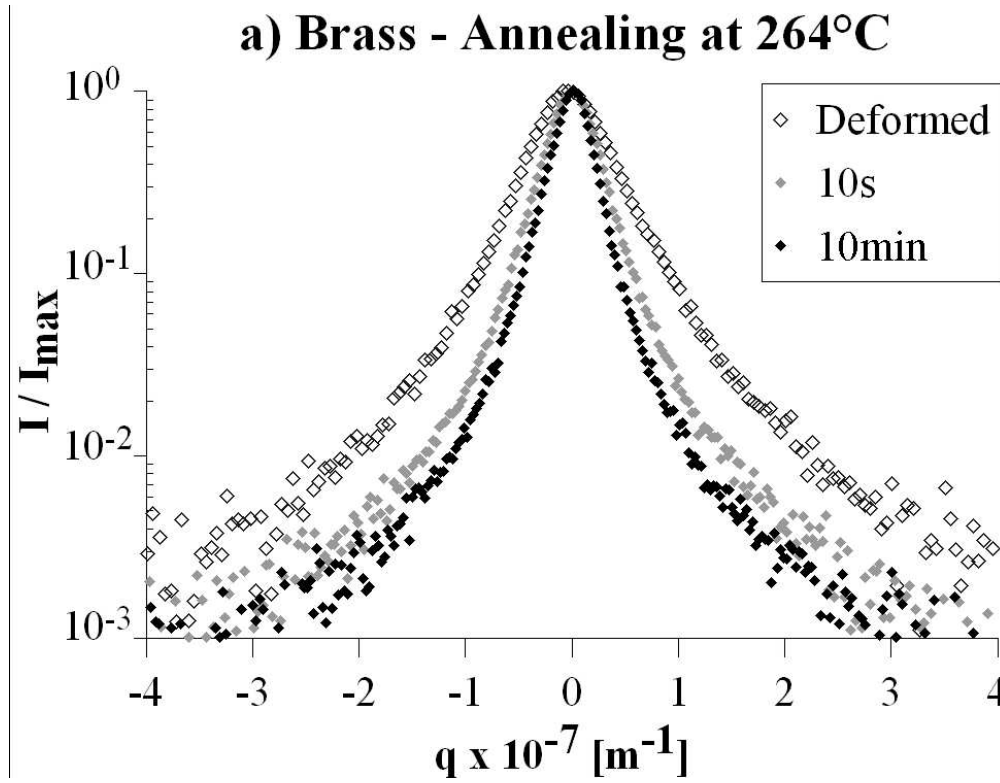
View Only



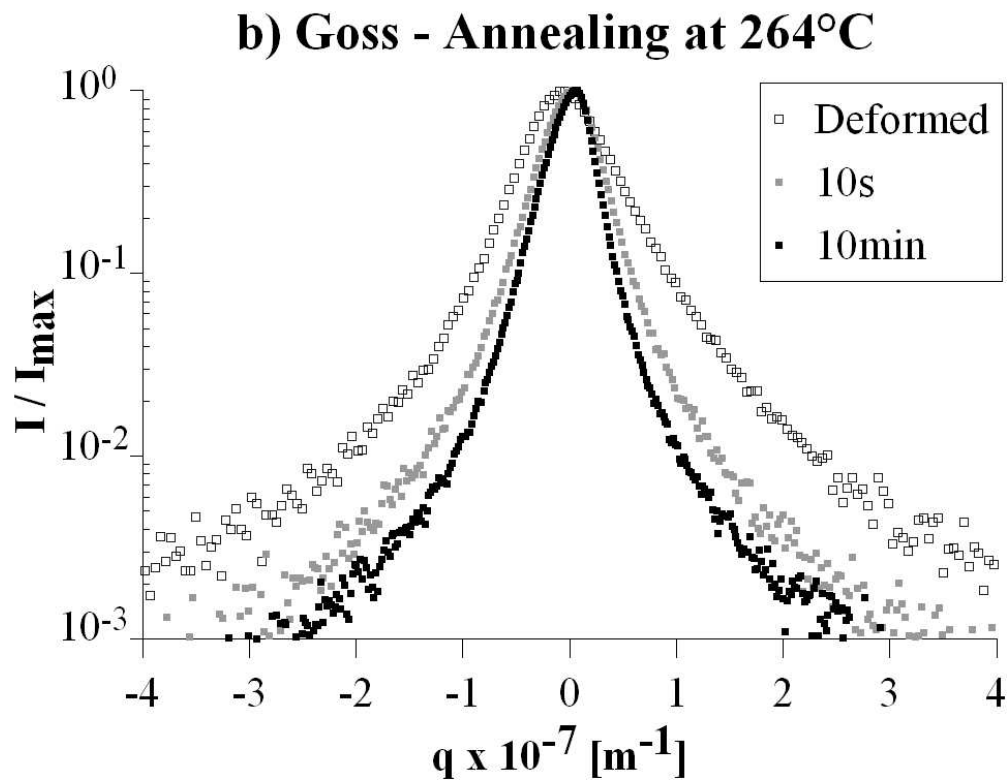
82x62mm (300 x 300 DPI)

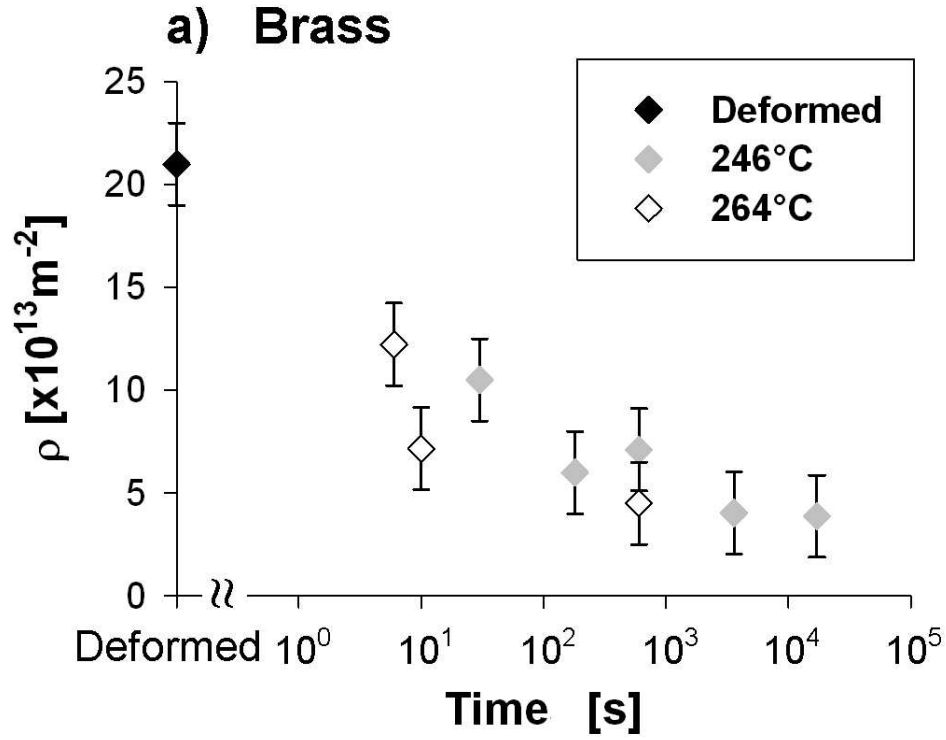
View Only

1  
2  
3  
4  
5  
6  
7  
8  
9  
10  
11  
12  
13  
14  
15  
16  
17  
18  
19  
20  
21  
22  
23  
24  
25  
26  
27  
28  
29  
30  
31  
32  
33  
34  
35  
36  
37  
38  
39  
40  
41  
42  
43  
44  
45  
46  
47  
48  
49  
50  
51  
52  
53  
54  
55  
56  
57  
58  
59  
60

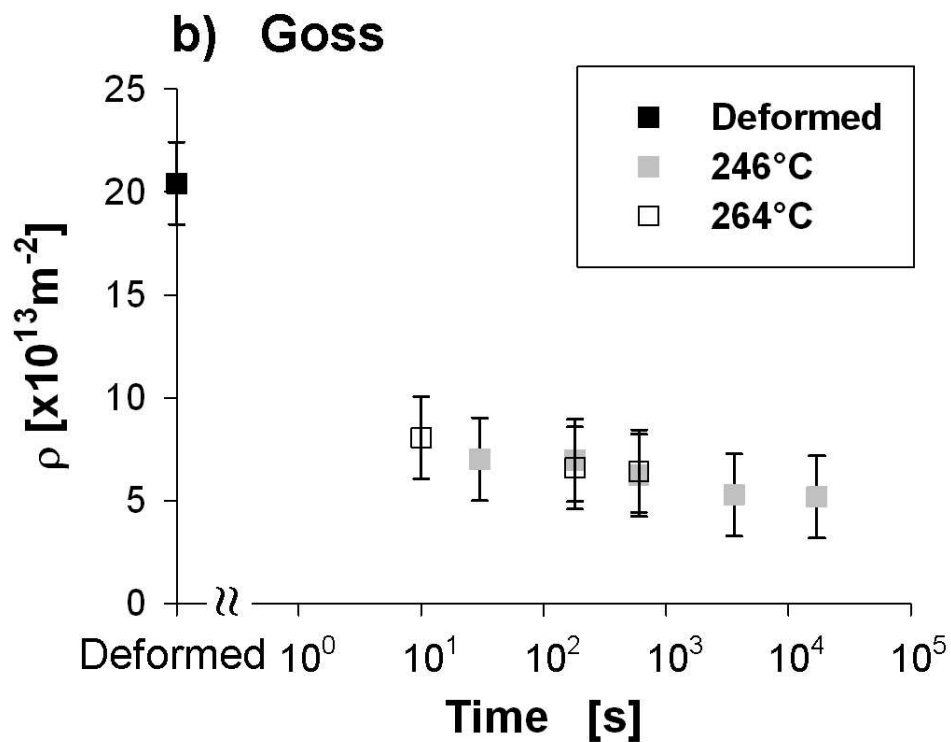


82x63mm (300 x 300 DPI)



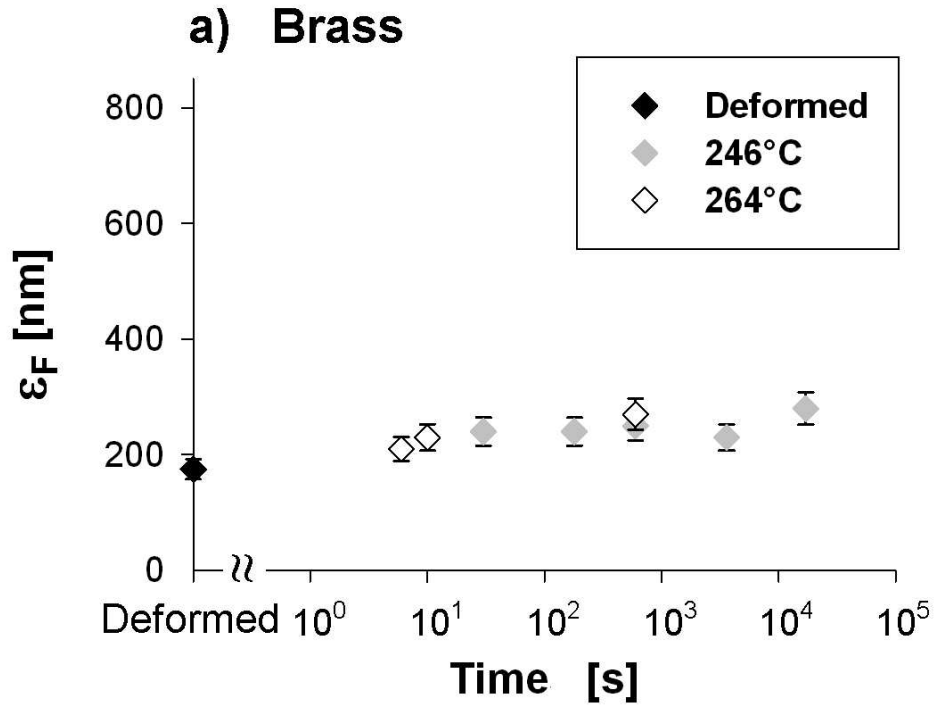


90x74mm (300 x 300 DPI)

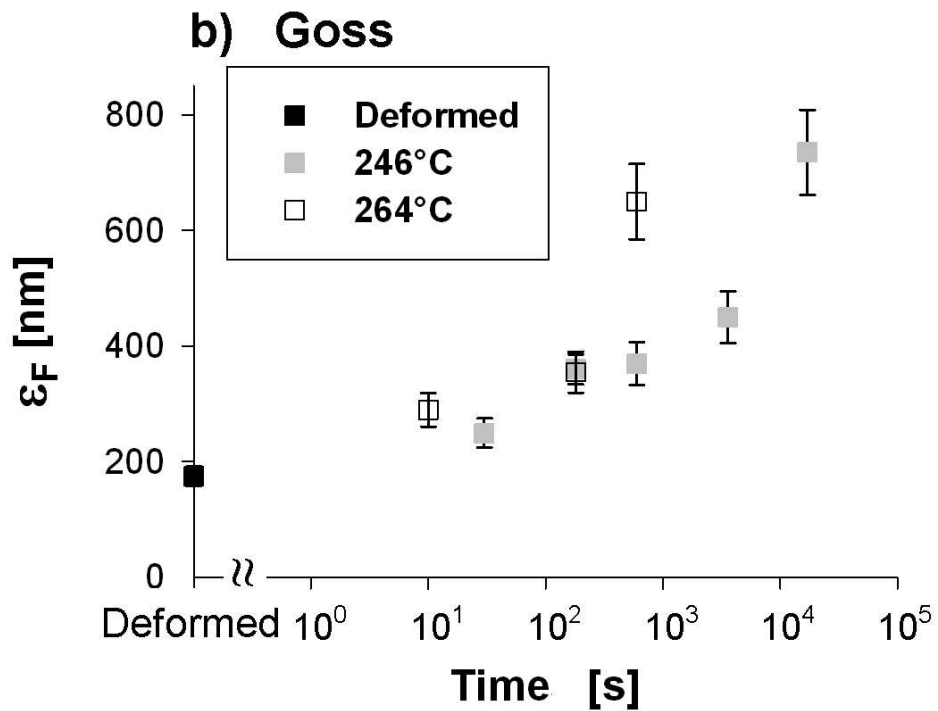


90x74mm (300 x 300 DPI)

1  
2  
3  
4  
5  
6  
7  
8  
9  
10  
11  
12  
13  
14  
15  
16  
17  
18  
19  
20  
21  
22  
23  
24  
25  
26  
27  
28  
29  
30  
31  
32  
33  
34  
35  
36  
37  
38  
39  
40  
41  
42  
43  
44  
45  
46  
47  
48  
49  
50  
51  
52  
53  
54  
55  
56  
57  
58  
59  
60



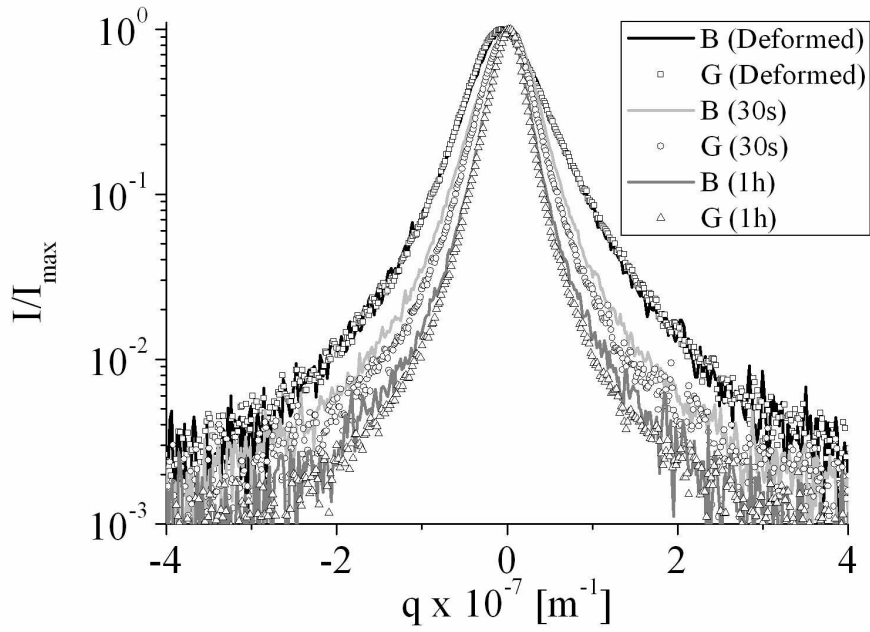
94x74mm (300 x 300 DPI)



94x74mm (300 x 300 DPI)



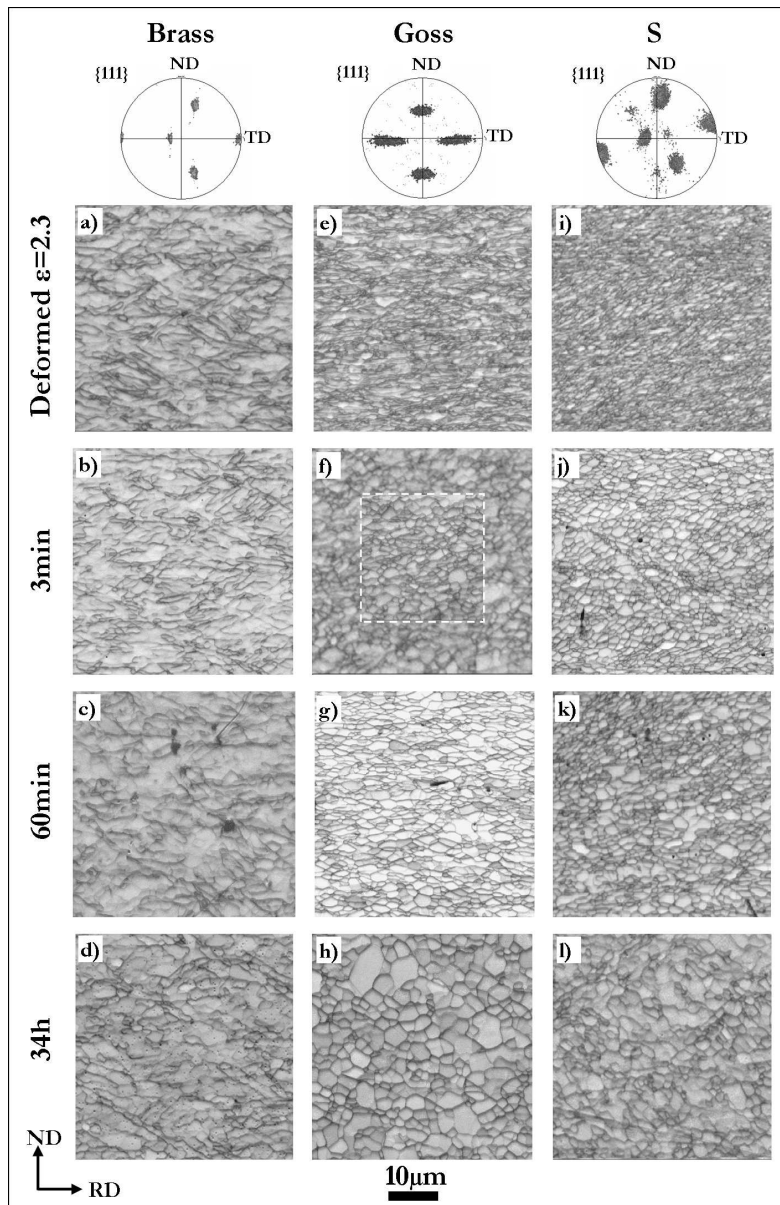
1  
2  
3  
4  
5  
6  
7  
8  
9  
10  
11  
12  
13  
14  
15  
16  
17  
18  
19  
20  
21  
22  
23  
24  
25  
26  
27  
28  
29  
30  
31  
32  
33  
34  
35  
36  
37  
38  
39  
40  
41  
42  
43  
44  
45  
46  
47  
48  
49  
50  
51  
52  
53  
54  
55  
56  
57  
58  
59  
60



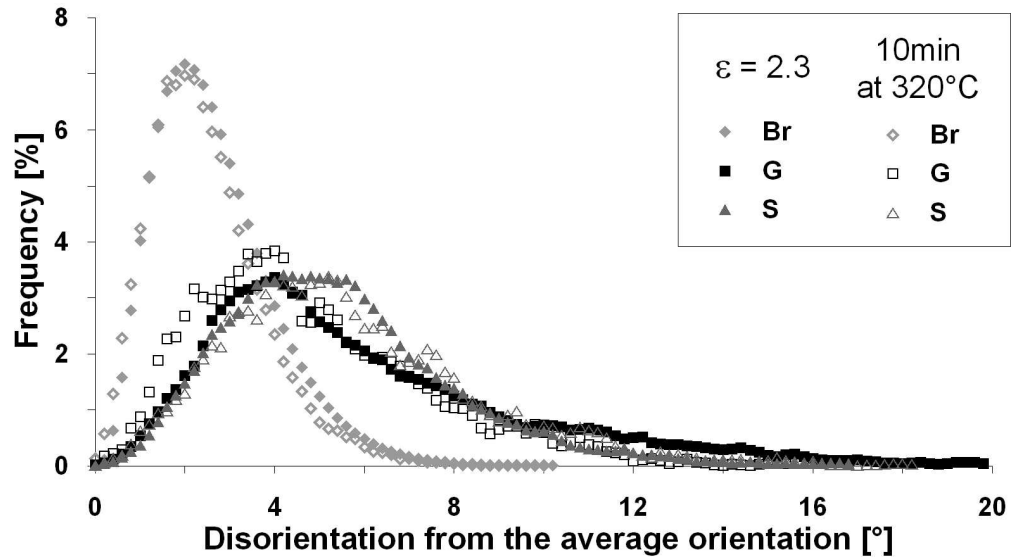
288x201mm (150 x 150 DPI)

view Only

1  
2  
3  
4  
5  
6  
7  
8  
9  
10  
11  
12  
13  
14  
15  
16  
17  
18  
19  
20  
21  
22  
23  
24  
25  
26  
27  
28  
29  
30  
31  
32  
33  
34  
35  
36  
37  
38  
39  
40  
41  
42  
43  
44  
45  
46  
47  
48  
49  
50  
51  
52  
53  
54  
55  
56  
57  
58  
59  
60



149x229mm (240 x 240 DPI)

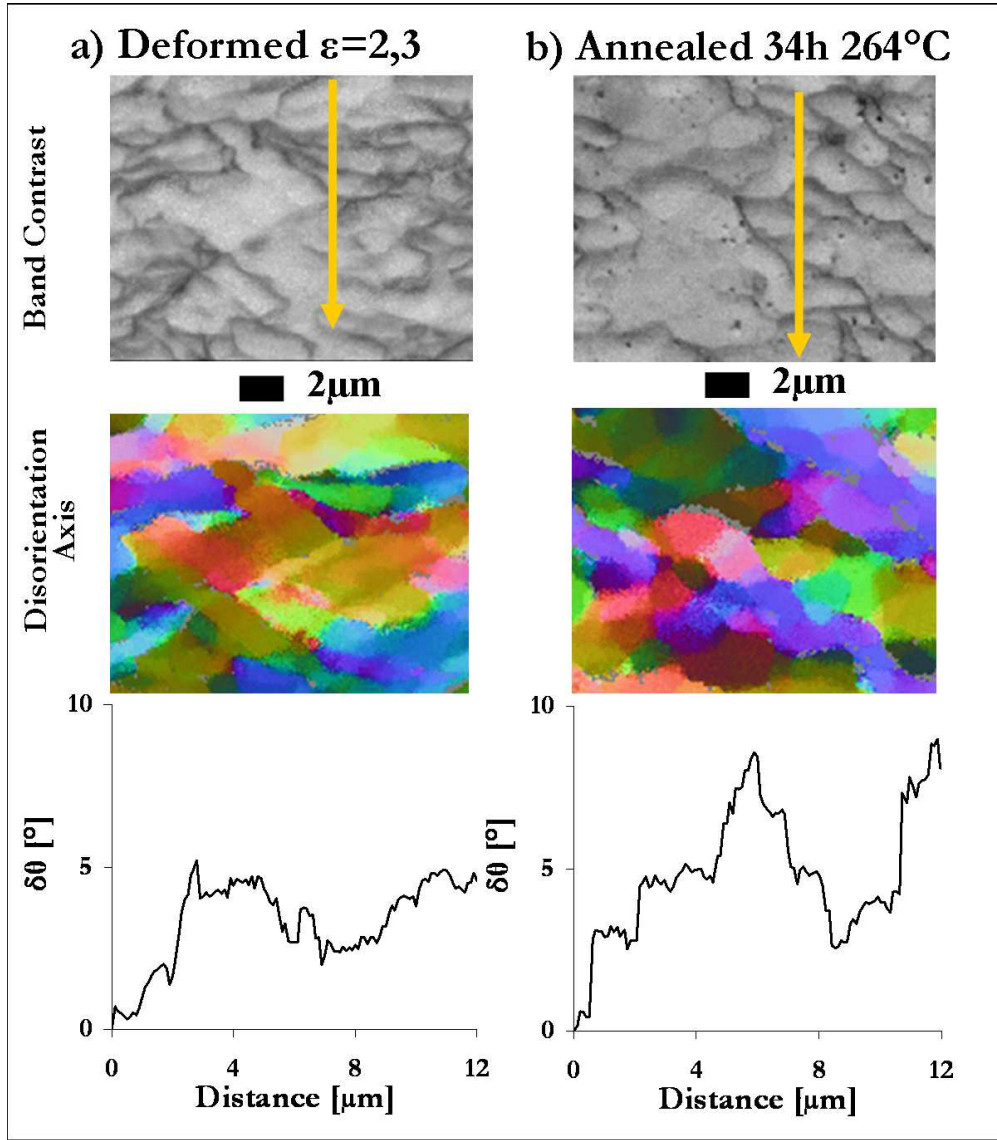


133x74mm (300 x 300 DPI)

Review Only

1  
2  
3  
4  
5  
6  
7  
8  
9  
10  
11  
12  
13  
14  
15  
16  
17  
18  
19  
20  
21  
22  
23  
24  
25  
26  
27  
28  
29  
30  
31  
32  
33  
34  
35  
36  
37  
38  
39  
40  
41  
42  
43  
44  
45  
46  
47  
48  
49  
50  
51  
52  
53  
54  
55  
56  
57  
58  
59  
60

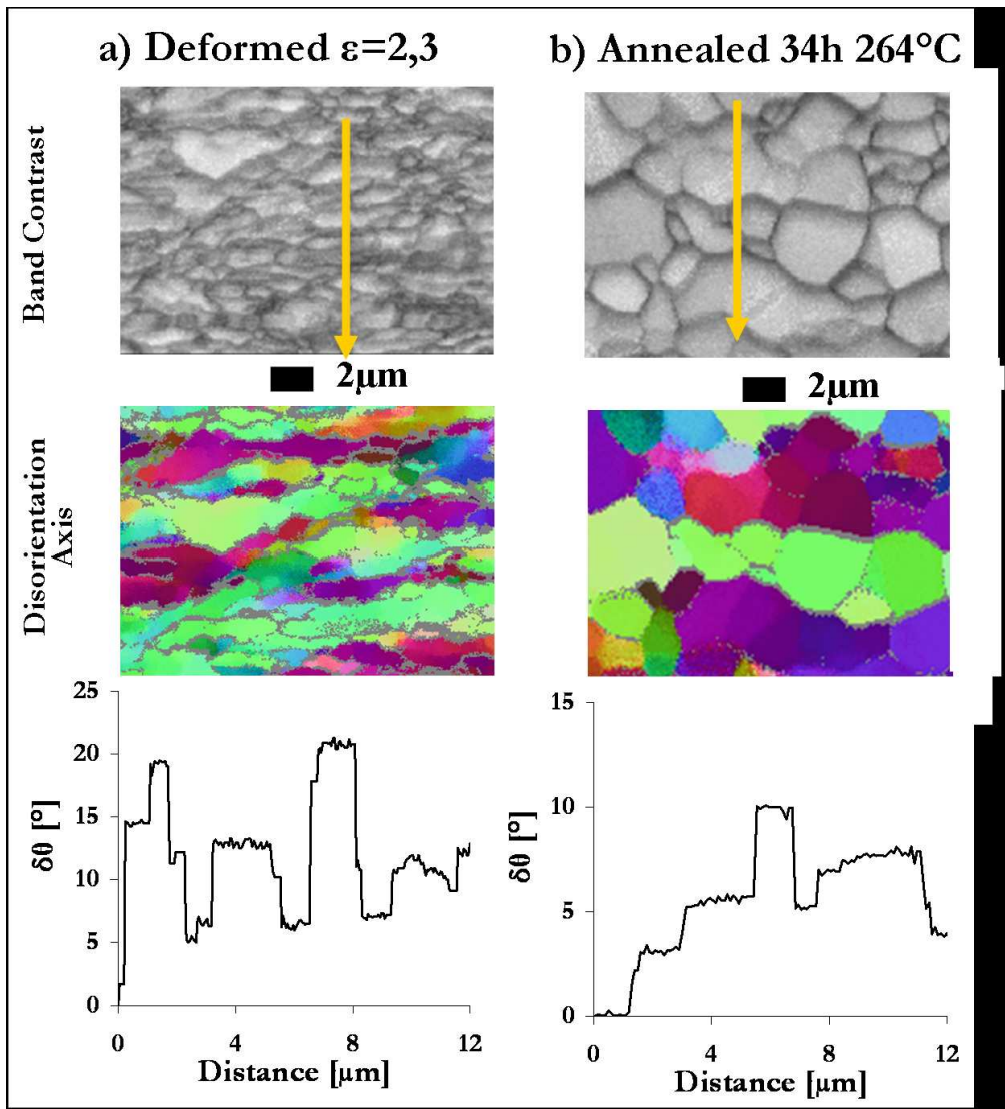
1  
2  
3  
4  
5  
6  
7  
8  
9  
10  
11  
12  
13  
14  
15  
16  
17  
18  
19  
20  
21  
22  
23  
24  
25  
26  
27  
28  
29  
30  
31  
32  
33  
34  
35  
36  
37  
38  
39  
40  
41  
42  
43  
44  
45  
46  
47  
48  
49  
50  
51  
52  
53  
54  
55  
56  
57  
58  
59  
60



127x144mm (240 x 240 DPI)



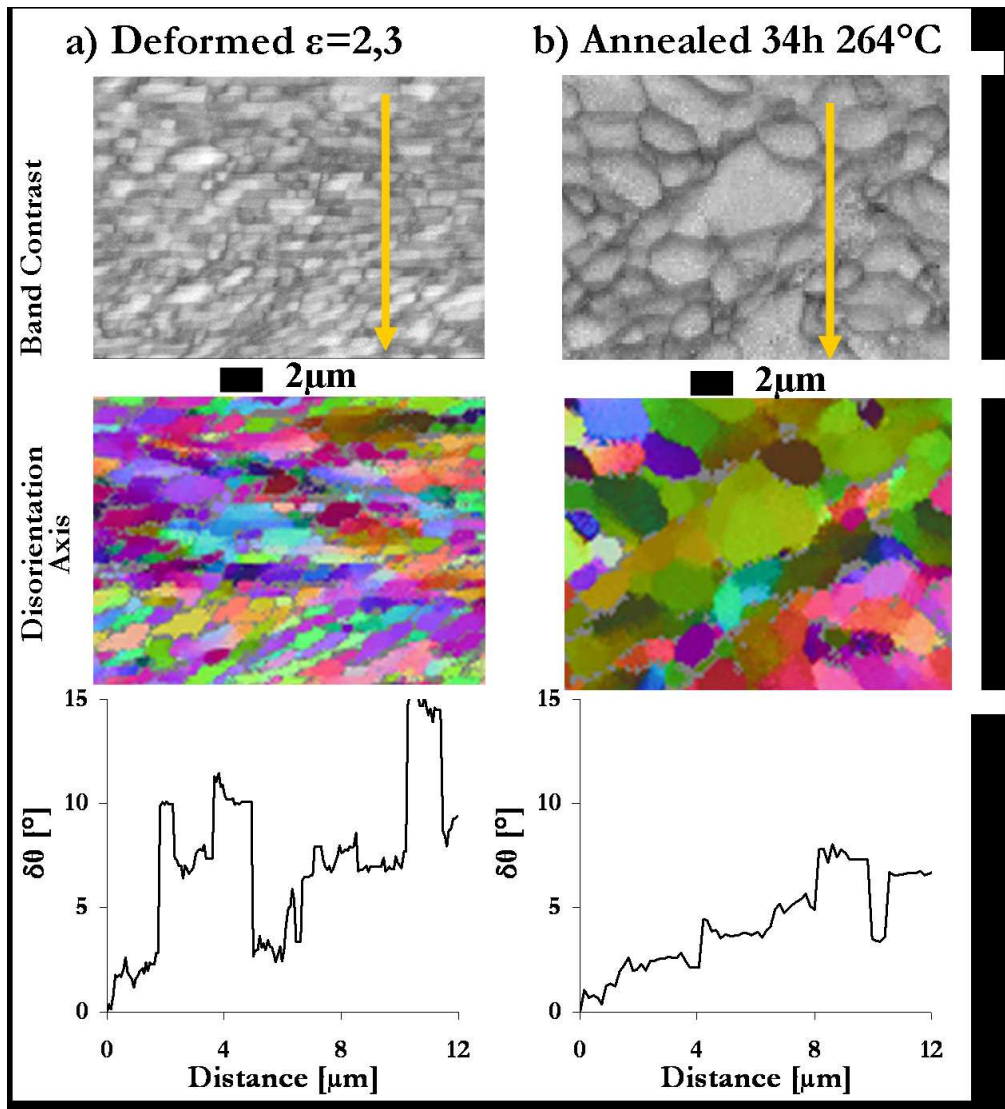
1  
2  
3  
4  
5  
6  
7  
8  
9  
10  
11  
12  
13  
14  
15  
16  
17  
18  
19  
20  
21  
22  
23  
24  
25  
26  
27  
28  
29  
30  
31  
32  
33  
34  
35  
36  
37  
38  
39  
40  
41  
42  
43  
44  
45  
46  
47  
48  
49  
50  
51  
52  
53  
54  
55  
56  
57  
58  
59  
60



131x144mm (240 x 240 DPI)



1  
2  
3  
4  
5  
6  
7  
8  
9  
10  
11  
12  
13  
14  
15  
16  
17  
18  
19  
20  
21  
22  
23  
24  
25  
26  
27  
28  
29  
30  
31  
32  
33  
34  
35  
36  
37  
38  
39  
40  
41  
42  
43  
44  
45  
46  
47  
48  
49  
50  
51  
52  
53  
54  
55  
56  
57  
58  
59  
60



132x146mm (240 x 240 DPI)

